RSC Advances

PAPER

View Article Online
View Journal | View Issue

CrossMark click for updates

Cite this: RSC Adv., 2016, 6, 21193

Published on 15 February 2016. Downloaded by Gazi Universitesi on 30/03/2016 02:47:58.

Performance of mesoporous silicas (MCM-41 and SBA-15) and carbon (CMK-3) in the removal of gas-phase naphthalene: adsorption capacity, rate and regenerability†

Yingshu Liu,[a] Ziyi Li,*[a] Xiong Yang,[a] Yi Xing,*[b] Chuenjinn Tsai,[c] Quan Yang,[a] Zhanying Wang[a] and Ralph T. Yang[d]

Received 21st December 2015
Accepted 12th February 2016

DOI: 10.1039/c5ra27289k

www.rsc.org/advances

The adsorption isotherms of naphthalene on three typical mesoporous adsorbents, mesosilicas MCM-41 and SBA-15, and mesocarbon CMK-3 were determined by column tests at 125 °C, with feed concentrations ranging from 7.63×10^{-5} to 4.64×10^{-2} mol m^{-3} (1.88 to 1140 ppm). The Langmuir model and constant-pattern wave propagation model were found to well fit the isotherms and the breakthrough curves, respectively. Regenerabilities of the mesoporous samples and a benchmark activated carbon (AC) were characterized based on thermogravimetric analysis (TGA). The results show mesoporosity significantly reduced the internal mass-transfer resistance, contributing to facile desorption and to fast adsorption kinetics shown by high overall mass-transfer rate coefficient following the order of: CMK-3 > SBA-15 > MCM-41. Micropore–mesopore coexisting structures present in CMK-3 and SBA-15 facilitated the adsorption at very low concentrations due to micropore-filling, while greater surface hydrophobicity and micropore abundance on CMK-3 exhibited larger affinity for nonpolar naphthalene, rendering the highest adsorption capacity (1.014 mol m^{-3}) among all sorbents including ACs. SBA-15 showed higher regenerability with a desorption temperature below 440 K, owing to the weaker binding and diffusion advantages contributed by the interconnectivity between primary mesopores.

1. Introduction

Polycyclic aromatic hydrocarbons (PAHs) in ambient air are of great concern currently because of their carcinogenic and mutagenic effects to humans[1,2] and contributions to the formation of particulate matter.[3,4] As a group of hazardous persistent organic pollutants, PAHs can be mainly emitted from anthropogenic sources such as engine exhausts,[5] incinerators[6] and industrial processes,[7] and will pose significant impacts on the environment even at extremely low concentrations.[8] For these reasons, there is an increasing demand to control PAHs emissions using appropriate technologies.

Various control technologies for low-concentration PAHs have been proposed and practiced in recent years, including adsorption,[9] chemical oxidation,[10] photocatalytic oxidation.[11] Adsorption on porous material is considered one of the most competitive technologies for gas-phase PAHs abatement because of its advantages of high efficiency, simplicity and flexibility.[12,13] Generally, adsorbents have high surface areas, micropore volumes and hydrophobic surfaces for the removal of gaseous pollutants.[14] Previous researches mainly focused on activated carbons (ACs). Mastral *et al.* once reported the adsorption of naphthalene, phenanthrene, and pyrene over 16 carbon materials.[15] Hu *et al.* have demonstrated the adsorption performance of naphthalene on different kinds of ACs by using tar model compounds.[16] However, traditional ACs suffer from limited interconnectivity between micropores and irregular and defective pore structures, which serve to reduce mass transfer efficiency and diffusion kinetics, ultimately restricting the access of large molecules to the internal adsorption sites as well as the regenerability in thermal desorption.[17–19] It is of significance to study new effective adsorbents for the removal of PAHs.

Over past few decades, the discovery of well-ordered mesoporous materials has attracted intense interest due to their high surface area, uniform pore size distribution, tunable pore structure and promising applications as adsorbents for

[a]School of Mechanical Engineering, University of Science and Technology Beijing, Beijing, 100083, China. E-mail: masterlazy@163.com; Fax: +86-10-62334210; Tel: +86-10-62332751

[b]School of Civil and Environmental Engineering, University of Science and Technology Beijing, Beijing, 100083, China. E-mail: xing_bkd@163.com; Fax: +86-10-62347649; Tel: +86-10-62332206

[c]Institute of Environmental Engineering, National Chiao Tung University, University Road, Hsinchu, 30010, Taiwan

[d]Department of Chemical Engineering, University of Michigan, Ann Arbor, Michigan 48109-2136, USA

† Electronic supplementary information (ESI) available. See DOI: 10.1039/c5ra27289k

Published on 15 February 2016. Downloaded by Gazi Universitesi on 30/03/2016 02:47:58.

environmentally hazardous compounds.[20] Two typical mesoporous silicas, MCM-41 with long range ordering giving rise to one-dimensional (1D) mesoporous channels[21] and SBA-15 with 2D hexagonal array of mesopore–micropore coexisting pore structures,[22] have been found to exhibit high hydrothermal stability and good adsorption performance for volatile organic compounds (VOCs).[23] Previous studies have indicated that the materials with bimodal pore size distribution (SBA-15) have high affinity for various VOCs due to their complementary micropores, which are favorable to the diffusion process.[24] Produced by pyrolysis of hydrocarbons adsorbed in the typical mesosilica matrices, ordered mesoporous carbons (OMCs), for example CMK-3 derived from SBA-15, have been considered as the next generation of adsorbents which are inert, stable, light, and mainly hydrophobic.[25] OMCs generally present higher affinity with larger microporosity and stronger hydrophobic interaction with organic compounds, rendering greater adsorption capacity as compared to conventional ACs.[26,27] It has been well recognized that mesoporous adsorbents offer excellent structural features to adsorb large organic molecules.[28] Thus far, knowledge about gas-phase PAHs adsorption on them is still scarce. This highlights the need to access corresponding investigations on mesoporous materials for broadening their environmental applications.

Naphthalene with two fused benzene rings is the simplest form of PAHs, which is considered representative for PAH in the industrial flue gases. It has been extensively shown that the adsorption of naphthalene as a nonpolar planar molecule on hydrophobic materials are mainly physical adsorption[29] and is reversible at low concentrations.[30] Texture properties of the adsorbents (*e.g.* pore size and distribution) play major roles in naphthalene adsorption whereas surface chemistries are supposed to be relatively indifferent,[31] although surface chemistries for functionalized adsorbents could make differences *via* the H-bonding[32] or other polarizable interactions.[33] Mastral *et al.* noted that the active sites on ACs should not influence the adsorption of low polarity molecules,[34] and that PAH adsorption mainly depends on the porous texture although their studied adsorbents showed great differences in surface chemistry.[9] Recently, Yang *et al.* found the morphology of adsorbents played an important role in the adsorption for aromatic compounds including naphthalene on carbon-based composite adsorbents, suggesting the electron–donor–acceptor (EDA) interaction contributed substantially.[35] Naphthalene with π-electron-rich property and flat conformation could be subject to π–π EDA interactions as a reversible chemical bond on CMK-3.[36] Thus far, no studies have been conducted to systematically compare adsorptive removal performance of gaseous naphthalene on mesoporous adsorbents, particularly originated from different geometrical structures and texture properties. Therefore, much more research is needed for a better understanding of the molecular interactions of mesoporous adsorbents and PAH contaminants.

In the present study, the adsorptive characteristics of gaseous naphthalene on MCM-41, SBA-15 and CMK-3, to be specific, the adsorption equilibrium derived from isotherms and the adsorption mass transfer rate from breakthrough curves were obtained, with the comparison to previous studies regarding naphthalene or other VOC on traditional adsorbents. Temperature programmed desorption (TPD) for naphthalene on each mesoporous sample and a benchmark AC were recorded. Accordingly the regenerabilities for the sorbate–sorbent pairs were evaluated and compared on the basis of desorption kinetic triplet, *i.e.* activation energy, pre-exponential factor, and kinetic model, determined by applying analytical methods to the TPD curves.

2. Materials and method

2.1 Adsorbents and adsorbate

Mesoporous silicas, MCM-41 [21] and SBA-15 [37] (purchased from Nanjing XFNANO Materials Tech Co., Ltd.) and the mesoporous carbon, CMK-3 [38] (purchased from Nanjing JCNANO Materials Tech Co., Ltd.) were used as the adsorbents. These materials were prepared using well established procedures.[21,37,38] Gas-phase naphthalene generated by heating the naphthalene solid (>99 wt%, Aldrich, USA) at a constant temperature was used as the adsorbate.

2.2 Characterization of adsorbents

Low-angle X-ray diffraction (XRD) patterns of the three samples were recorded on an X-ray diffractometer (Rigaku, D/max-2500, Japan) using Cu Kα radiation ($\lambda = 0.1541$ nm) at 40 kV and 200 mA in the 2θ range of 0.5–10° with a scanning rate of 0.5° min^{-1}. The surface morphologies of the samples were obtained using transmission electron microscopy (TEM, JEOL JEM-2010, Japan). The TEM samples were ultrasonicated in ethanol solution and were then dispersed on carbon film supported 200 mesh copper grids. The N_2 isotherms were measured with Autosorb-1 (Quantachrome, USA) at 77 K. Prior to measurements, all of the samples were degassed at 393.15 K for 12 h. The pore structure parameters including the specific surface area (S_{BET}), the pore volume, the mesopore diameter ($d_{p,NLDFT}$) based on the nonlocal density functional theory (NLDFT) method and the pore wall thickness (T_w) are listed in Table S2.† The Brunauer–Emmett–Teller (BET) method was applied to calculate the specific surface area using N_2 adsorption data in a relative pressure range from 0.05 to 0.25. The pore size distributions extending over micro- and meso-pore ranges for the samples were calculated from the N_2 isotherms based on NLDFT method which is also able to give the mesopore and micropore volumes.[39] The total pore volumes were estimated according to N_2 uptake at a relative pressure (P/P_0) of 0.99.

2.3 Adsorption experiment

The adsorption experiment was carried out with a laboratory-scaled apparatus as shown in Fig. 1. The experiment was designed to simulate practical removal of PAHs from hot combustion or process gases. The gas-phase naphthalene was obtained by sublimating the solid naphthalene contained in a quartz cylindrical saturator (6.0 mm ID) into a stream of pure helium (10 mL min^{-1}) as the carrier gas. The saturator was set inside a water bath capable of providing a constant temperature

 This journal is © The Royal Society of Chemistry 2016

Published on 15 February 2016. Downloaded by Gazi Universitesi on 30/03/2016 02:47:58.

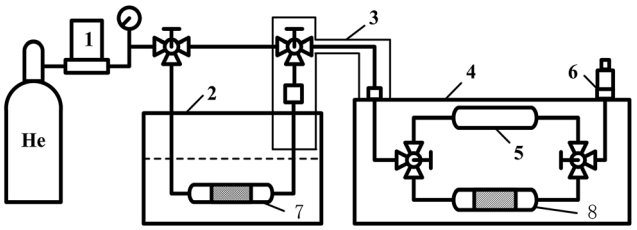

Fig. 1 Schematic diagram of adsorption experimental system: (1) mass flow controller; (2) water bath; (3) heating tape; (4) chromatographic furnace; (5) dummy column; (6) FID detector; (7) adsorbate saturator; (8) adsorption column.

from −10 to 60 °C to generate constant concentrations of the adsorbate. A pair of adsorbent tube and dummy tube made of quartz glass with the inner diameter of 3.0 mm, length of 12.5 mm, was kept inside a chromatographic furnace. The adsorption temperature inside the furnace was accurately controlled at 125 ± 0.1 °C. 10–30 mg of the adsorbent (180–250 μm) mixed with 870–1000 mg of same-sized inert sand was fixed in the adsorbent tube, obtaining a bed length of 11 mm. The dummy tube was packed with inert sand bed of the same length as that in the adsorbent tube, which showed negligible adsorption capacity of naphthalene manifested by the blank test. The experimental conditions and main parameters are summarized in Table S1 of the ESI.†

Prior to each adsorption test, the feed concentrations of naphthalene, C_0 (mol m^{-3}), for the adsorbent tube were determined by passing the gas stream through the dummy tube and detecting the outlet concentration with a flame ionization detector (FID). The FID had been previously calibrated, as described in the ESI.† The value of C_0 at each selected generation temperature was determined as shown in Table S3.† When the measured concentration reached a stable level (C_0), the adsorption test was started by shifting the upstream and downstream three-way valves to let the gas flow through the adsorbent tube. The real-time naphthalene concentration, C (mol m^{-3}), in the outlet gas stream varying with the adsorption time, t (s), was recorded as the breakthrough curves. The adsorption capacity at certain feed concentration, W (mol kg^{-1}), was calculated by the numerical integration method:

$$W = \frac{Q}{w}\left(C_0 t_m - \int_0^{t_m} C\,dt\right) \quad (1)$$

where Q is the gas flow rate (mL min^{-1}); w is the adsorbent mass (mol g^{-1}); t_m is the adsorption time when the C reaches 95% of C_0 (min).

2.4 Breakthrough curve modeling

On the basis of the low-concentration feed gas and small gas velocity during the adsorption tests, a self-sharpening concentration wave of the adsorbate moving at a constant rate in column one could be assumed.[40] Accordingly, the constant-pattern wave propagation model[41] is able to give a reliable prediction for the breakthrough curves with an analytical solution.[42,43] Under the assumptions of negligible radial and axial dispersions, ideal plug flow pattern, uniform and constant temperature in the column, the governing equation for predicting the fixed bed dynamics is:

$$\varepsilon\frac{\partial C}{\partial t} + u_0\varepsilon\frac{\partial C}{\partial z} + \rho\frac{\partial q}{\partial t} = 0 \quad (2)$$

where ρ is the bulk density of the bed (kg m^{-3}); ε the bed porosity (m^3 m^{-3}); u_0 the interstitial velocity of the gas (m s^{-1}), t the operating time (s), and z the distance from the inlet of the mobile phase (m) and C and q are the naphthalene concentrations in the gas (mol m^{-3}) and stationary phases (mol g^{-1}), respectively.

The mass transfer between fluid and adsorbed phases is assumed to be very fast so that a "local equilibrium" is established, with the stationary phase being saturated as soon as the layer is in contact with the gas-phase wave front.[44] While the wave moves at a constant flow velocity, u_c, the gas-phase concentration can be expressed as a unique function of an adjusted time, τ, as:[45]

$$\tau = t - \frac{z}{u_c} \quad (3)$$

Substituting eqn (3) into eqn (2), we can obtain:

$$\left(1 - \frac{u_0}{u_c}\right)\frac{dC}{d\tau} + \frac{\rho}{\varepsilon}\frac{dq}{d\tau} = 0 \quad (4)$$

Applying the initial and boundary conditions to eqn (4) leads to:

$$\frac{q}{C} = \frac{q_0}{C_0} \quad (5)$$

where C_0 is the feed concentration in gas phase, and q_0 is the adsorbed naphthalene concentration in the stationary phase in equilibrium with C_0.

The term $\partial q/\partial t$ in eqn (2) represents the local adsorption rate, which can be described by the linear driving force model as:

$$\rho\frac{\partial q}{\partial t} = K_L\alpha(C - C^*) \quad (6)$$

where α is the mass-transfer area per unit volume of the bed, $\alpha = 6(1 - \varepsilon)/d_s$; K_L is the overall liquid-phase mass-transfer coefficient (m s^{-1}), and $K_L\alpha$ is called the volumetric mass-transfer coefficients (s^{-1}); C^* is the gas phase concentration in equilibrium with the solid phase concentration q^* (mol m^{-3}), in the adsorption isotherm relationship expressed by $q^* = f(C^*)$.

There are two other common expressions for the local adsorption rate in terms of the external and internal mass-transfer coefficients as $\rho\frac{\partial q}{\partial t} = k_f\alpha(C - C_s)$ and $\frac{\partial q}{\partial t} = k_p(q_s - q)$, respectively, where k_p is the internal mass-transfer coefficient in the stationary phase (s^{-1}); q_s is the concentration adsorbed at adsorbent surface (mol kg^{-1}); C_s is the gas concentration at the adsorbent exterior surface (mol m^{-3}); k_f is the external mass-transfer coefficient across the gas film on the exterior surface

Published on 15 February 2016. Downloaded by Gazi Universitesi on 30/03/2016 02:47:58.

of adsorbents (m s^{-1}), which can be determined by using the following correlation:[46]

$$Sh = (1.09/\varepsilon)Re^{1/3}Sc^{1/3} \quad (\text{for } 0.0001 < Re < 72) \tag{7}$$

where $Sh = (k_f d_s)/D_m$, $Re = (\rho_{He} u_0 d_s)/\mu$ and $Sc = \mu/(\rho_{He} D_m)$; μ is the dynamic viscosity of air (Pa s); ρ_{He} is the density of the carrier helium gas (kg m^3); and D_m is the molecule diffusion coefficient of naphthalene in helium gas which can be estimated by:[47]

$$D_m = \frac{\sqrt{\frac{1}{M_A} + \frac{1}{M_{He}}} \times T^{3/2} \times 5.36 \times 10^{-5}}{P\left(V_A{}^{1/3} + V_{He}{}^{1/3}\right)^2} \tag{8}$$

where the molecular weights of the adsorbate (naphthalene) M_A = 128 g mol^{-1}, and of helium M_{He} = 4 g mol^{-1}; the molar volumes of naphthalene V_A = 125 cm^3 mol^{-1}, and of helium V_{He} = 2.88 cm^3 mol^{-1}; the pressure P = 101.3 (kPa) and temperature T = 398.2 K. It should be noted that the relationship between the overall mass-transfer coefficient and the individual mass-transfer coefficients could be given by:[44]

$$\frac{1}{K_L \alpha} = \frac{1}{k_f \alpha} + \frac{C_0}{k_p \rho q_0} \tag{9}$$

Substituting eqn (5) into eqn (6) gives:

$$\frac{\rho q_0}{C_0}\frac{dC}{d\tau} = K_L \alpha\left[C - f^{-1}(Cq_0/C_0)\right] \tag{10}$$

Considering $\tau - \tau_{1/2} = [t - (z/u_c)] - [t_{1/2} - (z/u_c)] = t - t_{1/2}$ with boundary conditions $C = C_0/2$ at $\tau = \tau_{1/2}$, eqn (8) can be rearranged and integrated by replacing τ with t as:

$$t = t_{1/2} + \frac{\rho q_0}{K_L \alpha C_0}\int_{1/2}^{x} \frac{1}{C - f^{-1}(Cq_0/C_0)} dx \tag{11}$$

where x is the dimensionless outlet adsorbate concentration defined as $x = C/C_0$, and $t_{1/2}$ is the adsorption time when x reaches 50%. The breakthrough curve can be described with eqn (11) based on specific equilibrium adsorption relationship, for instance, upon the Langmuir isotherm as:

$$t = t_{1/2} + \frac{\rho q_0}{K_L \alpha C_0}\left[\ln 2x + \frac{1}{1 + bC_0} \ln \frac{1}{2(1 - x)}\right] \tag{12}$$

where b is the Langmuir constant. Once the value of $K_L\alpha$ are determined from curve fitting using eqn (12), with the value of k_f obtained from eqn (7), the internal mass-transfer coefficient k_p can be calculated from eqn (9).

2.5 Temperature programmed desorption (TPD)

Desorption of the naphthalene on the adsorbents were evaluated by the TPD technique with a thermogravimetric analyzer (TGA) (Q500, TA Instruments, New Castle, DE, USA), in the temperature range of 293–850 K at four heating rates (β = 8, 12, 16 and 20 K min^{-1}). A coconut-shell-based AC (AC_{CS}) (ST1000, Nantong Carbon Co., Ltd., China) was added as a reference in the test for the comparison with the mesoporous samples. The naphthalene-loaded samples for TGA tests were obtained by soaking 0.12 ± 0.01 g of each sorbents into methanol (10 g) solution dissolved with 0.23 ± 0.01 naphthalene solids. After 48 hour's loading, 20 ± 1 mg of each naphthalene-loaded sample was placed into the TGA sample holder. The TPD was then started under pure-helium flowing at a rate of 20 mL min^{-1}, and the curves of desorption rates as a function of temperature were recorded.

3. Results and discussion

3.1 Properties of adsorbents

Powder low-angle XRD patterns of MCM-41, SBA-15 and CMK-3 are depicted in Fig. 2. MCM-41, SBA-15 and CMK-3 display three well-defined peaks, which can be indexed as (1 0 0), (1 1 0) and (2 0 0) diffractions, confirming a 2D hexagonal arrangement of mesopores ($p6m$).[28,48] The d spacing values of the (100) peaks of MCM-41, SBA-15 and CMK-3 are 3.85, 8.65 and 8.24 nm, respectively, which are obtained from Bragg's law, $n\lambda = 2d_{110}$-sin 2θ, where n = 1, and λ is 0.1541 nm (wavelength of the Cu Kα X-ray). The corresponding XRD peaks of MCM-41 are shifted to a higher due to the smaller hexagonal unit cell size ($a_0 = 2d_{110}/\sqrt{3}$) compared with SBA-15 and CMK-3. This could also be manifested by the TEM characterization for each sample as shown in Fig. 3. As CMK-3 is the negative replica structure of SBA-15,[49] they show similar peak diffraction angles. The intensity of (1 0 0) reflection is smaller for MCM-41 and SBA-15 as compared to that of the CMK-3, indicating more ordered structures on CMK-3.

The porosity of the three mesoporous samples were investigated by nitrogen adsorption–desorption isotherms along with the corresponding pore size distributions as shown in Fig. 4. All of the adsorption isotherms, with a sharp capillary condensation step at intermediate relative pressure, feature type IV according to the IUPAC classification, indicative of uniform mesopores.[50] The pore structure parameters including S_{BET}, $d_{p,NLDFT}$, T_w and pore volumes are listed in Table 2. T_w was

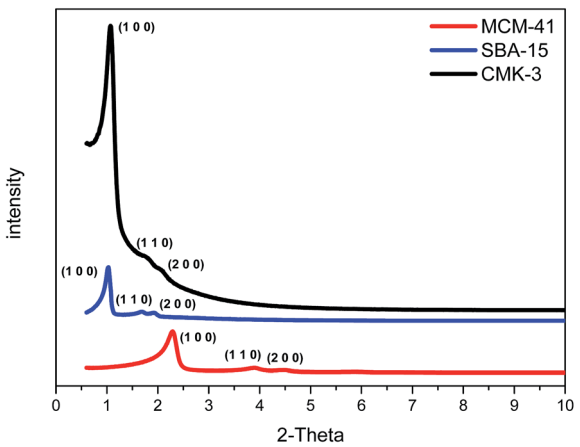

Fig. 2 Powder X-ray diffraction patterns of MCM-41, SBA-15 and CMK-3.

 This journal is © The Royal Society of Chemistry 2016

Published on 15 February 2016. Downloaded by Gazi Universitesi on 30/03/2016 02:47:58.

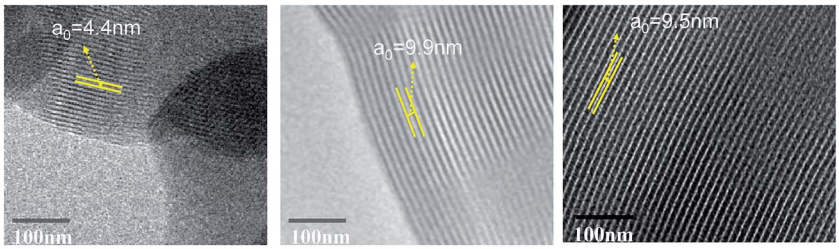

Fig. 3 TEM images of (a) MCM-41; (b) SBA-15 and (c) CMK-3.

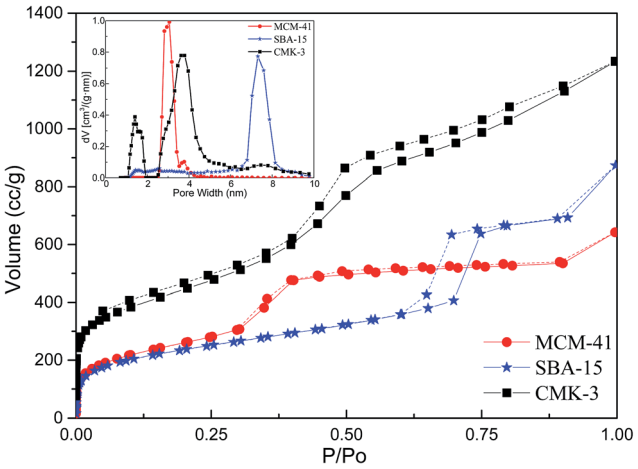

Fig. 4 77 K nitrogen adsorption/desorption isotherms and the corresponding pore size distributions of MCM-41, SBA-15 and CMK-3.

calculated by taking the difference between a_0 and $d_{p,NLDFT}$, $T_w = a_0 - d_{p,NLDFT}$, with the assumption that mesopores in all samples are presented in a perfect hexagonal structure.[51] The S_{BET} of CMK-3 (1575.9 $m^2\ g^{-1}$) is higher than those of SBA-15 (816.5 $m^2\ g^{-1}$) and MCM-41 (961.5 $m^2\ g^{-1}$), due to the micropores formed during the carbonization process. In addition, CMK-3 has much larger volume of total pore, mesopore and particularly micropore as compared to the other two samples.

Significant differences in pore size distributions of the three samples can be observed. Both SBA-15 and CMK-3 contain microporous and mesoporous structures, whereas MCM-41 exhibits only one peak at 2.8 nm with no microporosity. CMK-3 and SBA-15 present different pore sizes with similar values of a_0. This is because the CMK-3 was prepared by using SBA-15 material as template, the pores and the pore walls of which become the framework and the pores of CMK-3, respectively. As seen from Table 1, T_w of SBA-15 (2.68 nm) is smaller than its pore size (7.31 nm), resulting the smaller pore size of CMK-3 (3.79 nm) than its T_w (5.73 nm).[52]

3.2 Napthalene adsorption isotherms

The adsorption capacities of naphthalene at different feed concentrations for MCM-41, SBA-15 and CMK-3 were obtained from their breakthrough curves. The adsorption isotherm of naphthalene at 125 °C on each sample can be seen in Fig. 5. For the low equilibrium concentrations (<0.06 mol m^{-3}) in our experiments, all isotherms are of type I representing monolayer adsorptions. The adsorption capacity increased and tended to level off with increasing C_0. The Langmuir, Freundlich and Dubinin–Radushkevich (D–R) DR isotherm equations were employed to fit the adsorption isotherm data. The equilibrium parameters and regression coefficients (R^2) of the models are summarized in Table 2. Langmuir equation was found to best fit the experimental data with higher R^2 as compared to other equations, and was used to estimate the saturated adsorption capacity (q_m) of naphthalene on each sample. As seen from Table 3, q_m of the adsorbents followed the order of CMK-3 > SBA-15 > MCM-41, corresponding to the same order of the abundance of micropores.

The sharp initial rises of the adsorption isotherm at lower concentrations are due to micropore filling and the slopes of the plateau at higher concentrations could be associated with adsorption on the non-microporous surfaces.[53] The absence of micropores in MCM-41 resulted in low adsorption capacity, while SBA-15 with similar V_{meso} and S_{BET} as MCM-41 exhibited larger adsorption capacity because of its complementary micropores/small mesopores in walls of the primary mesopore channels. It should be noted that at the very lower equilibrium concentrations (<0.01 mol m^{-3}), CMK-3 shows substantially larger adsorption capacity as compared to SBA-15 and MCM-41. The high microporosity of CMK-3 facilitated the adsorption that mainly took place in micropores with sizes close to the naphthalene molecular size (0.62 nm [15]), enhancing the adsorption

Table 1 Textural properties of MCM-41, SBA-15 and CMK-3 derived from XRD and BET characterizations

Samples	S_{BET} ($m^2\ g^{-1}$)	V_p ($cm^3\ g^{-1}$)	V_{micro} ($cm^3\ g^{-1}$)	V_{meso} ($cm^3\ g^{-1}$)	$d_{p,NLD}$ (nm)	a_0 (nm)	T_w (nm)
MCM-41	961.5	0.91	0.001	0.91	3.06	4.45	1.39
SBA-15	876.5	1.01	0.038	0.97	7.31	9.99	2.68
CMK-3	1575.9	1.91	0.29	1.62	3.79	9.52	5.73

Published on 15 February 2016. Downloaded by Gazi Universitesi on 30/03/2016 02:47:58.

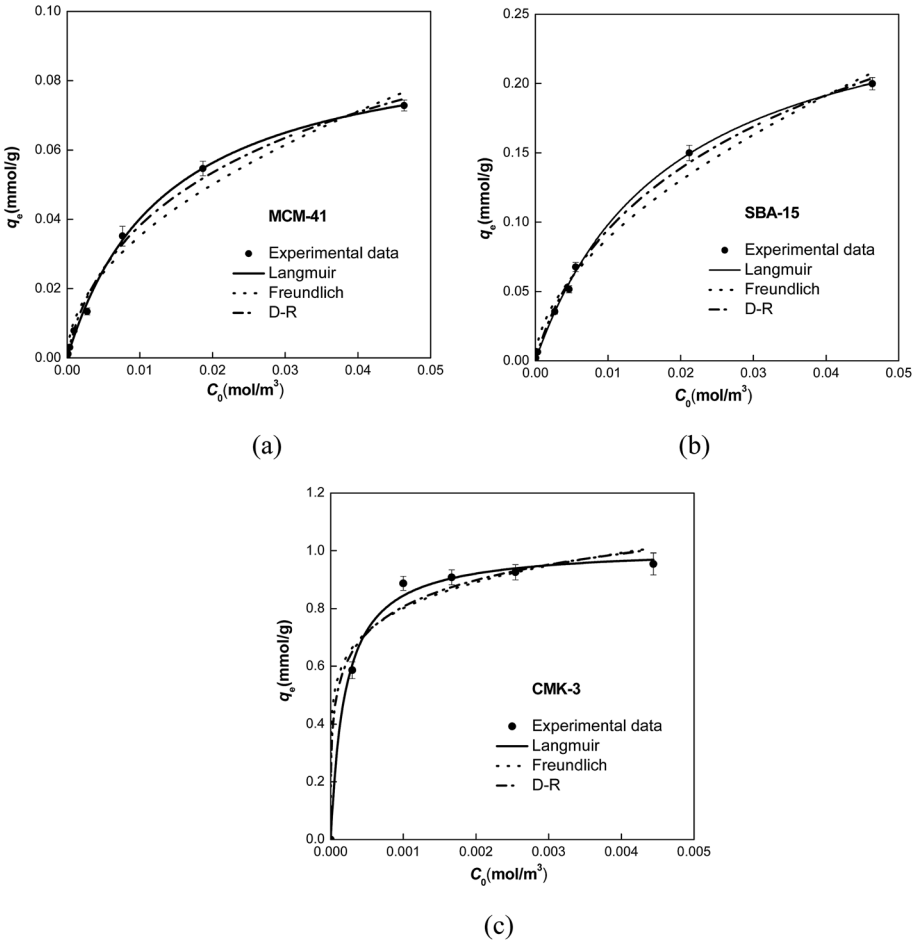

Fig. 5 Adsorption isotherms (at 125 °C) of naphthalene on (a) MCM-41; (b) SBA-15; (c) CMK-3.

potential due to the proximity of pore walls. These results are in accordance with previous conclusions that high PAHs adsorption capacity at low equilibrium concentrations is related to high micropore volumes.[13–16,54] On the other hand, carbon-based surfaces generally show stronger π–π interactions with aromatic rings due to the electron-depleted regions caused primarily by the surface defects formed in synthesis carbonization process as well as the π-electron-rich property and flat conformation of the aromatic adsorbates.[55,56]

A comparison of the adsorption capacity of CMK-3 may also be made with that of ACs. Mastral *et al.* studied adsorption of naphthalene on 16 ACs derived from different precursors ranging from coal to apricot stone.[15] The coal-based carbon (designated "CA-3") was the main sample being fully reported, including adsorption isotherm at 150 °C. At the lowest vapor

Table 2 Regression results of Langmuir, Freundlich and D–R isotherm equations

Model	Equation	Parameters	MCM-41	SBA-15	CMK-3
Langmuir	$q = \frac{q_m bC}{1+bC}$	q_m: saturated adsorption capacity (mol kg^{-1})	0.094	0.319	1.014
		b: Langmuir adsorption constant	72.02	43.29	5004.31
		R^2	0.996	0.997	0.995
Freundlich	$q = K_F C^{n_F}$	K_F: Freundlich adsorption capacity (mol kg^{-1})	0.372	1.356	2.334
		n_F: sorption intensity of adsorbents	0.52	0.592	0.155
		R^2	0.976	0.983	0.967
D–R	$\ln q = \ln q_{DR} - K_{DR}(\ln q)^2$	q_{DR}: DR adsorption capacity (mol kg^{-1})	0.127	0.416	1.423
		K_{DR}: a constant related to micropores	0.058	0.069	0.012
		R^2	0.985	0.989	0.975

 This journal is © The Royal Society of Chemistry 2016

Published on 15 February 2016. Downloaded by Gazi Universitesi on 30/03/2016 02:47:58.

Table 3 Fitting parameters of breakthrough curves using the constant-pattern wave model

Sample	C_0 (10^{-3} mol m^{-3})	$K_L\alpha$ (s^{-1})	$k_f\alpha$ (s^{-1})	k_p (s^{-1})	R^2
MCM-41	0.143	1.63	4.90×10^3	3.52×10^{-3}	0.967
	2.76	7.41	4.90×10^3	7.51×10^{-3}	0.959
SBA-15	0.143	2.71	7.20×10^3	2.62×10^{-3}	0.977
	2.76	9.74	7.20×10^3	9.95×10^{-3}	0.968
CMK-3	0.143	73.4	16.0×10^3	7.50×10^{-3}	0.976
	2.76	30.6	16.0×10^3	7.90×10^{-3}	0.925

concentration that was reported, 0.0015 mol m^{-3}, the adsorbed amount was 0.24 mol kg^{-1}, compared to 0.90 mol kg^{-1} for CMK-3 [Fig. 5(c)]. The estimated amount adsorbed for the AC with the highest capacity, "CA-8" (apricot stone-based), was approximately 0.61 mol g^{-1}, still significantly lower than that of CMK-3 even after considering the temperature dependence (125 *versus* 150 °C), based on a reasonable heat of adsorption. The reason for CMK-3 presenting more favorable adsorption of naphthalene as compared to the apricot stone-based carbon with an even higher micropore volume, could be largely associated with the unique features of CMK-3 which is more structurally well-defined and chemically homogeneous (with fewer surface oxides) than AC sorbents. The ordered carbon-rod matrices result in almost the entire mesopore surface atoms approach to naphthalene molecules and the available adsorption spaces include surfaces of both mesoporous matrices and inner cavities of the rods, which could be more than those on ACs with disordered structures.

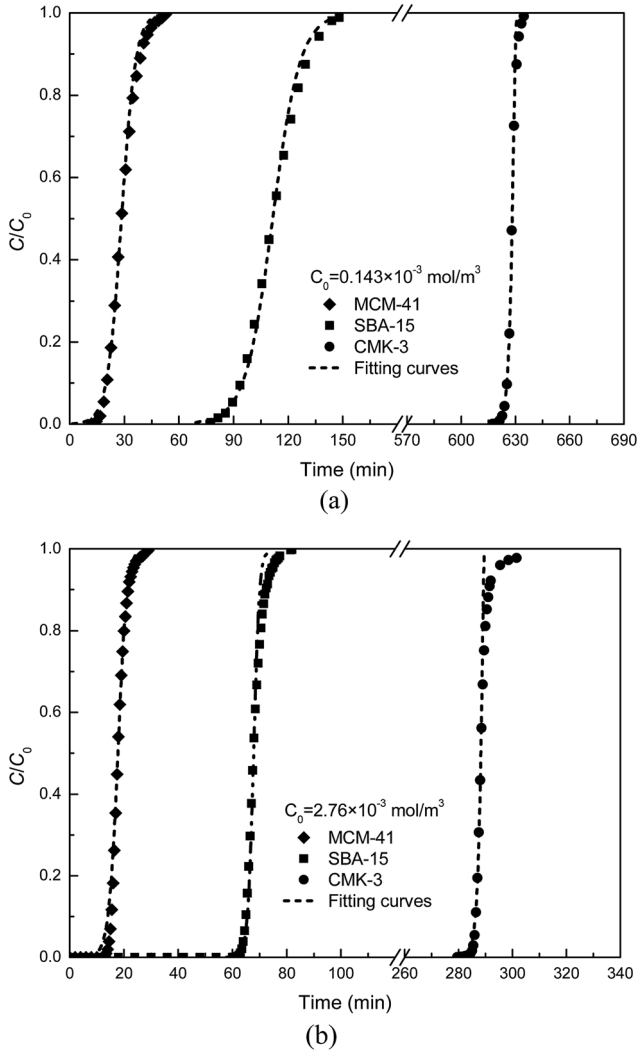

Fig. 6 Experimental and model-predicted breakthrough curves on mesoporous samples at the feed concentrations of (a) 0.143 × 10^{-3} mol m^{-3} and (b) 2.76 × 10^{-3} mol m^{-3}.

3.3 Naphthalene breakthrough dynamics

Once the adsorption isotherms of naphthalene over the samples were known in which Langmuir isotherm showed better correlation with experimental data, the constant-pattern wave model based on the Langmuir isotherm was used to predict the breakthrough curves of each investigated case. The value of half breakthrough time, $t_{1/2}$, and the volumetric mass-transfer coefficient, $K_L\alpha$, were determined by fitting the experimental breakthrough data to eqn (12) from the intercept and slope by plotting $[\ln 2x - 1/(1 + bC)\ln 2(1 - x)]$ *versus* t, respectively. Fig. 6(a) and (b) shows the experimental and model prediction breakthrough curves at C_0 of 0.143 × 10^{-3} mol m^{-3} (7.81 ppm) and 2.76 × 10^{-3} mol m^{-3} (67.9 ppm), respectively. Values of $t_{1/2}$, $K_L\alpha$, $k_f\alpha$ and k_p for each run are listed in Table 3.

The constant-pattern wave model gives good predictions for the experimental data, as evidenced by the relatively high values of R^2 along with the steep breakthrough slopes. For each sample $t_{1/2}$ is greater when the feed concentration is lower, indicating a longer equilibrium time for the adsorption under a smaller concentration gradient. For the same feed concentration, adsorbents with different porosity showed different values of $K_L\alpha$ following the sequence of CMK-3 > SBA-15 > MCM-41. The much higher values of $k_f\alpha$ compared to $K_L\alpha$ and k_p indicate the

Table 4 The changes of the T_p and α_p with heating rate and kinetic parameters obtained by Kissinger method

Samples	β (K min^{-1})	T_p (K)	α_p	E_a (kJ mol^{-1})	ln A (min^{-1})	R^2
MCM-41	8	383.4	0.506	64.44	15.26	0.999
	12	390.2	0.509			
	16	395.9	0.501			
	20	399.7	0.503			
SBA-15	8	369.9	0.593	59.11	14.27	0.996
	12	376.4	0.592			
	16	381.7	0.590			
	20	386.7	0.591			
CMK-3	8	423.0	0.315	74.31	16.14	0.994
	12	429.6	0.317			
	16	434.9	0.317			
	20	440.6	0.318			
AC_{CS}	8	515.3	0.428	97.99	17.77	0.993
	12	522.4	0.426			
	16	529.3	0.424			
	20	534.8	0.422			

Published on 15 February 2016. Downloaded by Gazi Universitesi on 30/03/2016 02:47:58.

mass-transfer resistance across the gas film on the external surface of adsorbent could be negligible. A sensitivity analysis was also performed to study the effects of mass-transfer parameters on the breakthrough curve, as shown in Fig. S1 and S2 of the ESI† for the sensitivity for k_f and k_p, respectively. It suggests that the internal mass transfer resistance is more important than the external mass transfer for the overall mass transfer of naphthalene adsorbed onto the mesoporous sample.

In comparison to previous studies for other organic gases with even smaller size on traditional adsorbents, the naphthalene adsorption on mesoporous adsorbents exhibit lower internal mass-transfer resistance with higher values of k_p,[44,57,58] which is summarized in Table S4 in the ESI.† This could be highly associated with the well-ordered mesoporous structures that offers smoother diffusions, as indicated by the previous conclusion that the narrower the microporosity, the slower the adsorption kinetics and the higher the height of the mass-transfer zone.[43] In addition, k_p tends to increase slightly (corresponding to steeper breakthrough curve) with increasing C_0 (Table 4), which is due to the increased driving force of mass-transfer with increasing intraparticle concentration gradient.[59] When the C_0 increases, the higher initial mass flux results in adsorbates shooting deep into the interior matrix of the sorbent, and more adsorption sites within the micropores could be occupied adequately.[60]

The micropores/small mesopores held by CMK-3 and SBA-15 contributed to their high overall mass-transfer efficiencies. Particularly for CMK-3, the presence of π–π interactions with the nonpolar naphthalene are supportive of the sorption affinity. According to eqn (9) neglecting the term $1/k_f\alpha$ on the

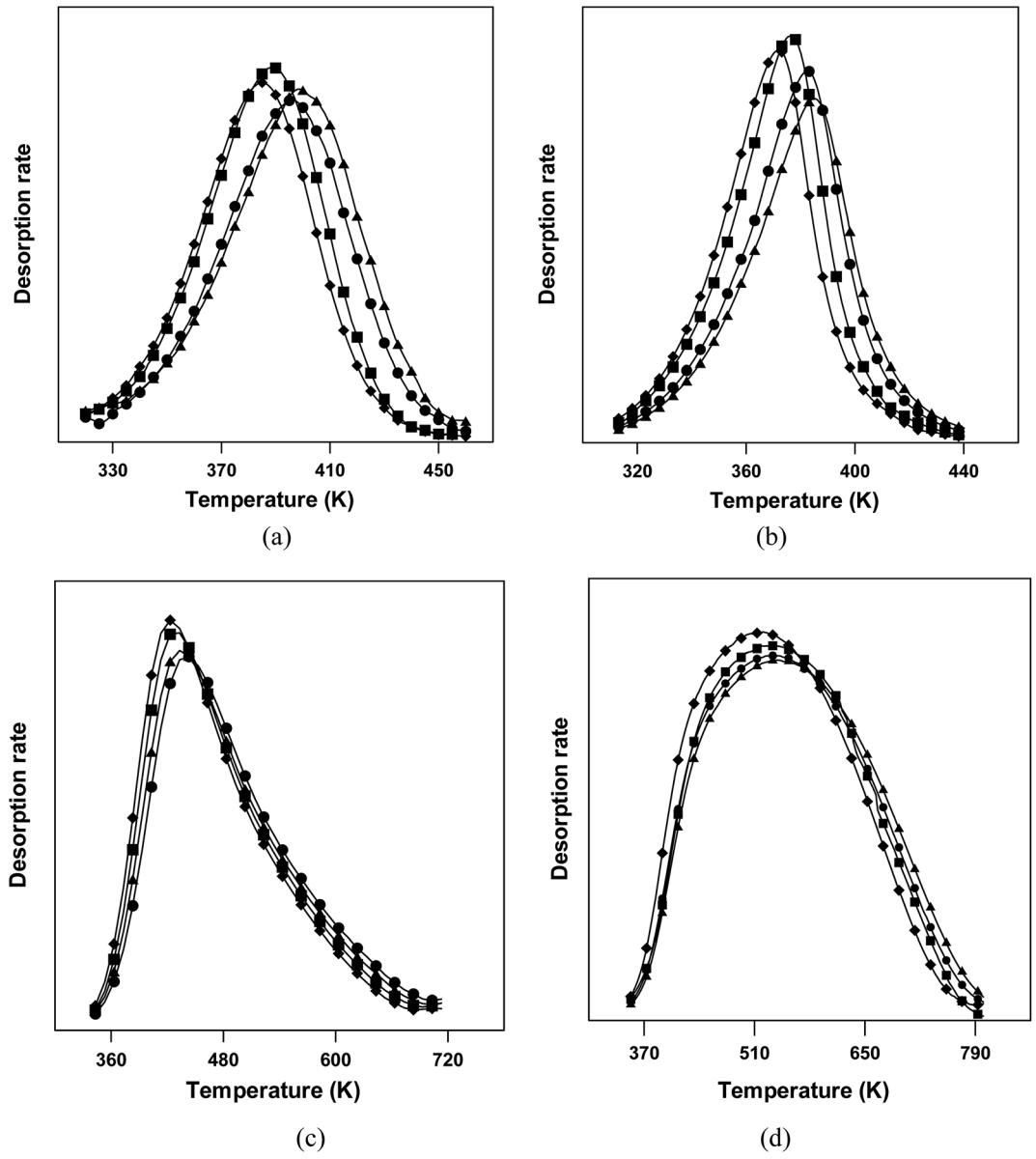

Fig. 7 TPD curves of naphthalene desorption rate at heating rate of ◆ 8 K min^{-1}, ■ 12 K min^{-1}, ● 16 K min^{-1} and ▲ 20 K min^{-1}, on (a) MCM-41; (b) SBA-15; (c) CMK-3 and (d) AC_{CS}.

 This journal is © The Royal Society of Chemistry 2016

Published on 15 February 2016. Downloaded by Gazi Universitesi on 30/03/2016 02:47:58.

right hand side, the value of $K_L\alpha$ varies not only with k_p but also the value of C_0/q_0 which depends on the adsorption isotherm relationship for the adsorbent. The change of $K_L\alpha$ is generally related to k_p when the value of C_0/q_0 varies little with the equilibrium concentration before the adsorption amount reaches saturated value. However in the case of CMK-3, the C_0/q_0 value is very small at the low feed concentration range due to the micropore-filling effect, and increases a lot at higher feed concentrations. The change of C_0/q_0 overwhelms that of k_p on CMK-3, thus leading to the decrease in $K_L\alpha$ which is still much higher than for other samples owing to its much larger adsorption capacity and surface hydrophobicity.

3.4 TPD study: sorbent regenerability

Regenerability is an important characteristic for adsorption applications in terms of sustainable and stable use of adsorbents. Higher desorption temperature will result in more energy cost and more demanding thermal stability of the material. The derivative thermogravimetric TPD curves of naphthalene on MCM-41, SBA-15, CMK-3 and AC_{CS} are presented in Fig. 7. The temperature, T_p, corresponding to the peak of each curve is listed in Table 4.

The desorption rates on three mesoporous adsorbents peak within the temperature range of 369.9–440.6 K, which is much lower than that of 515.3–534.8 K for AC_{CS}. Besides, the desorption peaks were also sharper on mesoporous adsorbents than on AC_{CS}, indicative of faster desorption. These results show the thermal regeneration advantage of mesoporous samples over AC_{CS}, which is largely contributed by the smoother diffusion for the adsorbate escaping from the surfaces on ordered mesoporous structures as compared to the disordered structures on the AC. To gain a deeper insight of the desorption nature, the desorption activation energy, E_a, and the pre-exponential factor, A with regard to the desorption kinetics,[61] were determined. The commonly used Kissinger method was employed to obtain these values:[62]

$$\ln\left(\frac{\beta}{T_p^2}\right) = \ln\left(\frac{AR}{E_a}\right) - \frac{E_a}{R}\left(\frac{1}{T_p}\right) \quad (13)$$

where E_a and $\ln A$ can be obtained by plotting $\ln(\beta/(T_p)^2)$ as a function of $1/T_p$, as listed in Table 4 along with the fitting correlation coefficient (R^2) for each run. The Kissinger method yields a reliable estimate of E_a especially when the degree of the desorption reaction at the maximum desorption rate, α_p, varies little with β,[63] which has been checked and verified from Table 4.

Both values of E_a and $\ln A$ follow the order of AC_{CS} > CMK-3 > MCM-14 > SBA-15. Higher E_a and $\ln A$ on the AC indicates a tighter sorption of naphthalene, which requires more energy as well as longer time for desorption, and *vice versa* for those mesoporous samples. As highlighted by our previous study,[61] the close fitting of adsorbate molecules in the abundant micropores on AC contributes significantly to strong binding energy. On the other hand, the n–π interaction as another type of EDA interaction, which exists between naphthalenes (π-electron acceptor) and n-electron donors, such as oxygen electron pairs of hydroxyl group and nitrogen electron pairs of amino group on the coconut shell AC,[64] might increase the overall adsorption binding.[35]

Despite having the similar textural characteristics of co-existing mesopores and micropores, CMK-3 did not present desorption as easy as SBA-15 did. This could be largely associated with the larger affinity with naphthalene on CMK-3 due to its higher surface hydrophobicity and the difference in micropore existing form on the two adsorbents. SBA-15 with micropore-embedded mesopore presents a 2-D cross-linked pore structure, which is believed to provide smoother and faster intraparticle diffusion for the naphthalene molecules being desorbed. CMK-3 with disordered micropores formed in the carbon rod structure could resist the desorption diffusion of adsorbates or might even hinder it due to the strong binding, although the microporosity is able to enhance the adsorption as shown above. This fact implies the importance of the presence of a proper composition of micropores (with proper pore sizes and amount) that are connected to the mesopores to achieve a balance between strong adsorption and easy desorption in practical use.

4. Conclusions

The adsorption performance and regenerability of gas-phase naphthalene on three typical mesoporous adsorbents, MCM-41, SBA-15 and CMK-3 were studied. The adsorption capacity was the highest for CMK-3 followed by SBA-15 and then by MCM-41. The structurally well-defined and chemically homogeneous CMK-3 also renders higher adsorption capacity compared to ACs based on literature results. The mesoporosity contributed to fast adsorption rate owing to the low internal mass transfer resistance. The mesoporous samples also showed significantly higher regenerability than the coconut shell AC sample (AC_{CS}), following the order of SBA-15 > MCM-14 > CMK-3 > AC_{CS}. The great desorption diffusion advantage on SBA-15 over other adsorbents benefits from its weaker sorption binding and micropores/small mesopores as interconnections between primary meso-channels. There exists a proper balance between strong adsorption and facile desorption regarding the micropores/small mesopores existing form and surface hydrophobicity, which merits further investigation.

In this study we systematically compare the adsorptive removal performance of mesoporous adsorbents in removal of gaseous naphthalene, particularly originated from different geometrical structures and texture properties. The results are of significance to provide guidance for the development of robust mesoporous adsorbents, to broaden the applications for their capturing or recycling gas-phase PAH compounds, and advance the understanding of their sorption behaviors in the environmental systems.

Acknowledgements

The financial support of the National Natural Science Foundation of China (Grant 51478038) is gratefully acknowledged.

Published on 15 February 2016. Downloaded by Gazi Universitesi on 30/03/2016 02:47:58.

References

1 P. Muller, B. Leece and D. Raha, *Part 1. Hazard Identification and Dose–Response Assessment*, Ministry of the Environment and Energy, Ottawa, Ontario, 1997.
2 Y. Cai, Z. H. Yan, N. Y. Wang, Q. Y. Cai and S. Z. Yao, *RSC Adv.*, 2015, **5**, 56189–56197.
3 Y. Liu, Y. Gao, N. Yu, C. Zhang, S. Wang, L. Ma, J. Zhao and R. Lohmann, *Chemosphere*, 2015, **134**, 52–59.
4 R. Lohmann, R. G. Lee, N. J. Green and K. C. Jones, *Atmos. Environ.*, 2000, **34**, 2529–2537.
5 L. C. Marr, T. W. Kirchstetter, R. A. Harley, A. H. Miguel, S. V. Hering and S. K. Hammond, *Environ. Sci. Technol.*, 1999, **33**, 3091–3099.
6 L. C. Wang, L. F. Lin and S. O. Lai, *J. Hazard. Mater.*, 2009, **168**, 438–444.
7 P. J. Kirton, J. Ellis and P. T. Crisp, *Fuel*, 1991, **70**, 1383–1389.
8 Y. X. Sun, Q. Hao, X. R. Xu, X. J. Luo, S. L. Wang, Z. W. Zhang and B. X. Mai, *Chemosphere*, 2014, **98**, 84–90.
9 A. M. Mastral, T. García, M. S. Callén, R. Murillo, M. V. Navarro and J. M. López, *Fuel Process. Technol.*, 2002, **7**, 373–379.
10 Y. Cai, Z. H. Yan, N. Y. Wang, Q. Y. Cai and S. Z. Yao, *RSC Adv.*, 2015, **5**, 56189–56197.
11 J. Sabate, J. M. Bayona and A. M. Solanas, *Chemosphere*, 2001, **44**, 119–124.
12 H. C. Zhou, Z. P. Zhong, B. S. Jin, Y. J. Huang and R. Xiao, *Chemosphere*, 2005, **59**, 861–869.
13 A. M. Mastral, T. García, R. Murillo, M. S. Callén, J. M. López and M. V. Navarro, *Ind. Eng. Chem. Res.*, 2003, **42**, 155–161.
14 C. Valderrama, X. Gamisans, X. De las Heras, A. Farran and J. L. Cortina, *J. Hazard. Mater.*, 2008, **157**, 386–396.
15 A. M. Mastral, T. García, M. S. Callén, M. V. Navarro and J. Galbán, *Environ. Sci. Technol.*, 2001, **35**, 2395–2400.
16 X. Hu, T. Hanaoka, K. Sakanishi, T. Shinagawa, S. Matsui, M. Tada and T. Iwasaki, *J. Jpn. Inst. Energy*, 2007, **35**, 707–711.
17 A. Aranda, M. V. Navarro, T. García, R. Murillo and A. M. Mastral, *Ind. Eng. Chem. Res.*, 2007, **46**, 8193–8198.
18 K. Kosuge, S. Kubo, N. Kikukawa and M. Takemori, *Langmuir*, 2007, **23**, 3095–3102.
19 W. Xin and Y. Song, *RSC Adv.*, 2015, **5**, 83239–83285.
20 A. Stein, *Adv. Mater.*, 2003, **15**, 763–775.
21 J. S. Beck, J. C. Vartuli, W. J. Roth, M. E. Leonowicz, C. T. Kresge, K. D. Schmitt and E. W. Sheppard, *J. Am. Chem. Soc.*, 1992, **114**, 10834–10843.
22 M. Kruk, M. Jaroniec, C. H. Ko and R. Ryoo, *Chem. Mater.*, 2000, **12**, 1961–1968.
23 L. T. Gibson, *Chem. Soc. Rev.*, 2014, **43**, 5163–5172.
24 H. Vinh-Thang, Q. Huang, M. Eic, D. Trong-On and S. Kaliaguine, *Langmuir*, 2005, **44**, 5094–5101.
25 Z. Wu and D. Zhao, *Chem. Commun.*, 2011, **47**, 3332–3338.
26 A. Vinu, K. Z. Hossain, G. S. Kumar and K. Ariga, *Carbon*, 2006, **44**, 530–536.
27 G. Yang, L. Tang, G. Zeng, Y. Cai, J. Tang, Y. Pang, Y. Zhou, Y. Liu, J. Wang, S. Zhang and W. Xiong, *Chem. Eng. J.*, 2015, **259**, 854–864.
28 B. Dou, Q. Hu, J. Li, S. Qiao and Z. Hao, *J. Hazard. Mater.*, 2011, **186**, 1615–1624.
29 Y. F. Jiang, X. F. Hu and U. Yves, *ACEM14*, Busan, Korea, August, 2014.
30 M. Sander and J. J. Pignatello, *Environ. Sci. Technol.*, 2005, **39**, 7476–7484.
31 Y. C. Chiang, P. C. Chiang and E. E. Chang, *J. Environ. Eng.*, 2001, **127**, 54–62.
32 K. Sun, J. Jin, M. Keiluweit, M. Kleber, Z. Wang, Z. Pan and B. Xing, *Bioresour. Technol.*, 2012, **118**, 120–127.
33 D. Zhu, B. E. Herbert, M. A. Schlautman and E. R. Carraway, *ACS National Meeting Book of Abstracts*, 2001, vol. 41, pp. 734–738.
34 A. M. Mastral, T. García, M. S. Callén, M. V. Navarro and J. Galban, *Energy Fuels*, 2001, **15**, 1–7.
35 X. Yang, J. Li, T. Wen, X. Ren, Y. Huang and X. Wang, *Colloids Surf., A*, 2013, **422**, 118–125.
36 Z. Li, Y. Liu, X. Yang, Y. Xing, C. J. Tsai, Z. Wang, Q. Yang and R. T. Yang, *Ind. Eng. Chem. Res.*, 2016, **55**, 1183–1191.
37 D. Y. Zhao, J. L. Feng, Q. S. Huo, N. Melosh, G. H. Fredrickson, B. F. Chmelka and G. D. Stucky, *Science*, 1998, **279**, 548–552.
38 R. Ryoo, S. H. Joo and S. J. Jun, *J. Phys. Chem. B*, 1999, **103**, 7743–7746.
39 P. I. Ravikovitch and A. V. Neimark, *J. Phys. Chem. B*, 2001, **105**, 6817–6823.
40 F. G. Helfferich and P. W. Carr, *J. Chromatogr., A*, 1993, **629**, 97–122.
41 F. G. Helfferich and G. Klein, *Multicomponent Chromatography: Theory of Interference*, Marcel Dekker, Inc., NewYork, 1970.
42 J. M. Chern and Y. W. Chien, *Water Res.*, 2002, **36**, 647–655.
43 E. Sabio, F. Zamora, J. Ganan, C. M. Gonzalez-Garcia and J. F. Gonzalez, *Water Res.*, 2006, **40**, 3053–3060.
44 X. Zhang, S. Chen and H. T. Bi, *Carbon*, 2010, **48**, 2317–2326.
45 M. D. LeVan, G. Carta and C. M. Yon, *Adsorption and ion exchange*, McGraw-Hill, Inc., New York, 1997.
46 C. J. Geankoplis, *Transport processes momentum heat and mass*, Allyn & Bac, Inc., 1983.
47 R. B. Bird, W. E. Stewart and E. N. Lightfoot, *Transport Phenomena*, Wiley, Inc., New York, 1960.
48 D. Zhao, J. Sun, Q. Li and G. D. Stucky, *Chem. Mater.*, 2000, **12**, 275–279.
49 A. Vinu, K. Z. Hossain, G. S. Kumar and K. Ariga, *Carbon*, 2006, **44**, 530–536.
50 Y. Zhai, B. Tu and D. Zhao, *J. Mater. Chem.*, 2009, **19**, 131–140.
51 C. T. Hung and H. Bai, *Chem. Eng. Sci.*, 2008, **63**, 1997–2005.
52 H. Wang, F. L. Lam, X. Hu and K. M. Ng, *Langmuir*, 2006, **22**, 4583–4588.
53 R. Murillo, T. Garcıa, E. Aylón, M. S. Callén, M. V. Navarro, J. M. López and A. M. Mastral, *Carbon*, 2004, **42**, 2009–2017.
54 T. Phuphuakrat, T. Namioka and K. Yoshikawa, *Appl. Energy*, 2010, **87**, 2203–2211.

 This journal is © The Royal Society of Chemistry 2016

Published on 15 February 2016. Downloaded by Gazi Universitesi on 30/03/2016 02:47:58.

55 G. D. Sheng, D. D. Shao, X. M. Ren, X. Q. Wang, J. X. Li, Y. X. Chen and X. K. Wang, *J. Hazard. Mater.*, 2010, **178**, 505–516.
56 S. M. Kozlov, F. Vines and A. Gorling, *Carbon*, 2012, **50**, 2482–2492.
57 C. Lorimier, A. Subrenat, L. Le Coq and P. Le Cloirec, *Environ. Technol.*, 2005, **426**, 1217–1230.
58 S. Brosillon, M. H. Manero and J. N. Foussard, *Environ. Sci. Technol.*, 2001, **35**, 3571–3575.
59 S. H. Lin and R. S. Juang, *J. Hazard. Mater.*, 2004, **113**, 195–200.
60 R. S. Juang and J. Y. Shiau, *J. Hazard. Mater.*, 1999, **70**, 171–183.
61 Z. Li, Y. Liu, X. Yang, Y. Xing, Z. Wang, Q. Yang and R. T. Yang, *Energy Fuels*, 2015, **29**, 5303–5310.
62 H. E. Kissinger, *Anal. Chem.*, 1957, **29**, 1702–1706.
63 S. Vyazovkin, A. K. Burnham, J. M. Criado, L. A. Pérez-Maqueda, C. Popescu and N. Sbirrazzuoli, *Thermochim. Acta*, 2011, **520**, 1–19.
64 Z. Li, Y. Liu, C. Zhang, X. Yang, J. Ren and L. Jiang, *Energy Fuels*, 2015, **29**, 6858–6865.